A nonlinear viscoelastic constitutive model for cyclically loaded solid composite propellant

Xin Tong[a,b], Jinsheng Xu[a], Issam Doghri[b,*], Marieme Imene El Ghezal[c], Anouar Krairi[d], Xiong Chen[a]

[a] *School of Mechanical Engineering, Nanjing University of Science & Technology, 210094 Nanjing, China*

[b] *Université catholique de Louvain, Institute of Mechanics, Materials and Civil Engineering, B-1348 Louvain-La-Neuve, Belgium*

[c] *e-Xstream Engineering, Axis Park-Building H, Rue Emile Francqui 9, B-1435 Mont-Saint-Guibert, Belgium*

[d] *Materials Innovation Institute (M2i), Van der Burghweg 1, 2628 CS DELFT, Netherlands*

Abstract

In this paper, a novel nonlinear viscoelastic constitutive model is proposed to describe the mechanical behavior of a polymer matrix composite (HTPB propellant). The model is built upon two stress-dependent nonlinear functions within the hereditary integral formulation of viscoelasticity. After implementation into a finite element code, the proposed model is utilized to simulate the stress-strain responses of cyclically loaded HTPB propellant. The results show that the model is capable of capturing the main characteristics of the hysteresis loops during fatigue process and good quantitative agreement is found under circumstances that self-heating effect is not evident.

This paper deepens the understanding of the nonlinear behaviors of composite propellant under cyclic loading.

*Corresponding author.

Email address: issam.doghri@uclouvain.be (Issam Doghri)

International Journal of Solids and Structures (2020), doi: https://doi.org/10.1016/j.ijsolstr.2020.04.011

Keywords: solid composite propellant, hysteresis loop, nonlinear viscoelasticity, finite element method

1. Introduction

As an energy-rich polymer matrix composite, solid composite propellant is extensively used to be the propulsive source of rockets and missiles. This type of solid propellant is exposed to severe working conditions, for instance, vibration inside a missile while conducting high-speed maneuver. In terms of the micro-structure, a solid composite propellant is composed of a polymer matrix binder (e.g. HTPB, NEPE) and mineral particles (e.g. aluminum, ammonium perchlorate) and its mechanical behavior is highly temperature-, strain rate- and strain- dependent (Xu et al., 2008; DeLuca et al., 2013). It is well recognized that composite propellants exhibit nonlinear behaviors (Jung and Youn, 1999; Tunç and Özüpek, 2016). The rotation and slippage of filler particles and interaction between binder and particles during the loading can contribute to nonlinear behavior of composite propellant. The evolution of micro-cracks and micro-voids are other major sources of nonlinearity in the mechanical response of composite propellant.

The response of a nonlinear viscoelastic material subject to complex loading history can be obtained from the solution of either an integral (e.g. Hinterhoelzl and Schapery, 2004) or a differential constitutive form (e.g. Müller et al., 2011). Among them, Schapery's single integral model (Schapery, 1969) is commonly applied to describe the nonlinear viscoelastic behavior of materials and it has already been implemented in finite element (FE) packages using several numerical schemes. Haj-Ali and Muliana (2004) and Huang et al.

(2007) have developed numerical algorithms for implementation of Schapery's model in finite element code ABAQUS. Then Muliana and Haj-Ali (2008) employed Schapery's formulation to model the mechanical behavior of polymers. Furthermore, Darabi et al. (2011), Al-Rub and Darabi (2012), and Darabi et al. (2012) coupled the nonlinear viscoelasticity model of Schapery with viscoplasticity or a visco-damage model to more accurately simulate the nonlinear mechanical response of the hot mix asphalt or asphaltic materials at various stress levels and temperatures.

In addition to phenomenological models, some micromechanical models exist for composite polymers. Brassart et al. (2009) proposed an extended Mori Tanaka homogenization scheme for finite strain modeling of debonding in particle-reinforced elastomers. They do take into account the particle/matrix debonding, but they assume a nonlinear elastic matrix response, and they consider no cyclic loading. Due to the different paths of loading and unloading, cyclically loaded polymers exhibit a hysteretic response, induced by the viscous stress that deviates from purely elastic domain. The nonlinear constitutive models cited above do not seem to be able to correctly reproduce the hysteresis loops under cyclic loading. More generally, few constitutive models focus on the simulation of cyclic stress-strain relationships, for which simulating the hysteresis loops is challenging (Drozdov, 2011; Krairi and Doghri, 2014; Guo et al., 2018). Recently, Tunç and Özüpek (2017) and Tunç et al. (2019) proposed a finite strain thermo-viscoelastic model coupled with a continuum damage model. They implemented it in a finite element software and validated it against experimental data for solid propellants under several loadings, including cyclic ones. In the latter case, good agreement was found between experimental data and model predictions. However, it seems that the authors considered experimental cyclic loads with single sign stresses, and not tension-compression cycles as will be our focus in the present work.

The main objective of this paper is to develop a general nonlinear viscoelastic material constitutive model for predicting the macroscopic behavior of solid composite propellant under cyclic loading conditions. The model is phenomenological, but could be extended in the future to be micromechanically-based and include debonding (Muliana and Haj-Ali, 2006). This paper is organized as follows: in Section 2, the formulation of the nonlinear viscoelastic constitutive model is presented, followed by the implementation of a numerical algorithm in Section 3. Then the parameter identification procedure and the validation of the constitutive model against the experimental data are described in Section 4. This research is discussed in Section 5. Finally, conclusions are drawn in Section 6.

Tensor notation is used throughout this paper. The spherical and deviatoric fourth order operators $\mathbb{I}^{vol}$ and $\mathbb{I}^{dev}$ are given by:

$$\mathbb{I}^{vol} \equiv \frac{1}{3}\boldsymbol{I} \otimes \boldsymbol{I};\ \mathbb{I}^{dev} \equiv \mathbb{I} - \mathbb{I}^{vol}$$

where the symbols $\boldsymbol{I}$ and $\mathbb{I}$ are the second and fourth order symmetric identity tensors, respectively. A colon (:) designates a tensor product contracted over two indices:

$$\boldsymbol{a} : \boldsymbol{b} = a_{ij}b_{ji};\ (\boldsymbol{C} : \boldsymbol{a})_{ij} = C_{ijkl}a_{lk}$$

where summation over a repeated index is assessed.

2. Model formulation

2.1. Nonlinear viscoelastic constitutive model

Schapery (1969) suggested describing the creep response of a viscoelastic material under isothermal condition with the following one-dimensional equation:

$$\varepsilon^{ve}(t) = \widehat{g}_0(\sigma)D_0\sigma(t) + \widehat{g}_1(\sigma)\int_0^t \triangle D(\psi(t)-\psi(\tau))\frac{\mathrm{d}\left(\widehat{g}_2(\sigma)\sigma(\tau)\right)}{\mathrm{d}\tau}\mathrm{d}\tau \qquad (1)$$

where D_0 and $\triangle D$ are instantaneous and transient components of creep compliance at linear viscoelasticity, respectively, and $\psi(t)$ is reduced time given by

$$\psi(t) = \int_0^t \frac{\mathrm{d}\xi}{a_\sigma(\sigma(\xi))} \qquad (2)$$

$\widehat{g}_0$, $\widehat{g}_1$, $\widehat{g}_2$ and a_σ are referred to be nonlinear functions that are dependent on stress variables with $\widehat{g}_0 = \widehat{g}_1 = \widehat{g}_2 = a_\sigma = 1$ when the material exhibits linear behavior wherein the stress is quite small. The nonlinear viscoelastic parameters can be determined from creep and recovery tests.

The nonlinear viscoelastic stress functions can be determined from creep and recovery tests as in Lai and Bakker (1995). Schapery's model has been extensively studied and used in the literature, and a few examples are given in the following. Lai and Bakker (1995) and Kim and Muliana (2009) added a viscoplastic part to the model by assuming an additive decomposition of the total strain into viscoelastic and viscoplastic parts. Lai and Bakker (1996) and Kim and Muliana (2009) presented a multi-axial extension of the original 1D model after adopting the assumption that the hydrostatic and deviatoric responses were uncoupled. They also proposed numerical algorithms for finite element implementation, with the hereditary integral updated at the end of each time interval by recursive computation. The effects of temperature and physical aging for isotropic nonlinear viscoelastic materials were also incorporated. However, the Shapery-type models cited above were not assessed with respect to cyclic tension-compression loading.

Motivated and guided by the aforementioned models, in this study, the three-dimensional constitutive model is formulated under the hypothesis of small perturbation and proposed as:

$$\boldsymbol{\sigma}(t) = \int_{-}^{t} \mathbb{C}^{ve}(t-\tau,\sigma) : \frac{\partial\left(g_1(\sigma)\boldsymbol{\epsilon}(\tau)\right)}{\partial\tau}\mathrm{d}\tau \tag{3}$$

where $g_1(\sigma)$ is a nonlinear function of stress history, to be discussed in subsection 2.2. $\mathbb{C}^{ve}$ is the fourth order viscoelastic relaxation tensor, and for isotropic and homogeneous material, $\mathbb{C}^{ve}$ is decomposed into:

$$\mathbb{C}^{ve}(t,\sigma) = 2G(t,\sigma)\mathbb{I}^{dev} + 3K(t,\sigma)\mathbb{I}^{vol} \tag{4}$$

where $G(t,\sigma)$ and $K(t,\sigma)$ are shear and bulk moduli, respectively.

We assume that the hydrostatic and deviatoric responses of the material are uncoupled. Thus, decomposing stress and strain as follows:

$$\begin{cases} \boldsymbol{\epsilon}(t) = \boldsymbol{\xi}(t) + \varepsilon_H(t)\boldsymbol{I} \\ \boldsymbol{\sigma}(t) = \boldsymbol{s}(t) + \sigma_H(t)\boldsymbol{I} \end{cases} \tag{5}$$

and using Equations (4) and Equation (5), Equation (3) could be rewritten as:

$$\begin{aligned} \boldsymbol{\sigma}(t) &= 2\int_{-}^{t} G(t-\tau,\sigma)\frac{\partial(g_1(\sigma)\boldsymbol{\xi}(\tau))}{\partial\tau}\mathrm{d}\tau + \left(3\int_{-}^{t} K(t-\tau,\sigma)\frac{\partial(g_1(\sigma)\varepsilon_H(\tau))}{\partial\tau}\mathrm{d}\tau\right)\boldsymbol{I} \\ &= \boldsymbol{s}(t) + \sigma_H(t)\boldsymbol{I} \end{aligned} \tag{6}$$

In practice, $G(t,\sigma)$ and $K(t,\sigma)$ are expressed as Prony series:

$$\begin{cases} G(t,\sigma) = G \quad + \sum\limits_{i=1}^{I} G_i \exp\left(-\frac{t}{\tau_i^G g_2(\sigma)}\right) \\ K(t,\sigma) = K \quad + \sum\limits_{j=1}^{J} K_j \exp\left(-\frac{t}{\tau_j^K g_2(\sigma)}\right) \end{cases} \tag{7}$$

where $g_2(\sigma)$ is a stress history-dependent function (to be presented in subsection 2.2), G , K represent elastic shear and bulk moduli, G_i, K_j represent shear and bulk relaxation weights and τ_i^G, τ_j^K represent shear and bulk relaxation times, respectively. We modified the classical Boltzmann-type integral in the strain history by introducing nonlinear history-dependent stress functions in the relaxation shear and bulk moduli. These functions $g_1(\sigma)$ and $g_2(\sigma)$ will be presented in the next subsection.

2.2. Nonlinear history-dependent stress functions

The core of the model lies in the selection of the nonlinear history-dependent stress functions $g_1(\sigma)$ and $g_2(\sigma)$. Haj-Ali and Muliana (2004) used general polynomial functions of the effective octahedral shear stress as the nonlinear parameters. Nevertheless, calibration of numerous parameters of their model was quite complicated and the role of each parameter remained unclear. In addition, validation of their model was limited to monotonic and uniaxial loadings, and no cyclic loading simulations were shown.

In the present study, $g_1(\sigma)$ and $g_2(\sigma)$ are assumed to follow respectively a power and an exponential form, both dependent on stress history:

$$\begin{cases} g_1(\sigma(t)) = 1 + k_1 \left\langle \frac{\sigma_{vM}^{\max} - \sigma_0}{\sigma_0} \right\rangle^{m_1} \\ g_2(\sigma(t)) = C_2 + (1 - C_2) \exp\left(-\left\langle \frac{\sigma_{vM}^{\max} - \sigma_0}{k_2 \sigma_0} \right\rangle^{m_2}\right) \end{cases} \tag{8}$$

where $\langle x \rangle$ is Macaulay bracket used to describe the ramp function:

$$\langle x \rangle = \begin{cases} x, x > 0 \\ 0, x \leqslant 0 \end{cases} \tag{9}$$

where k_1, m_1, k_2, m_2 and C_2 are material constants to be determined; σ_0 denotes the linear viscoelastic stress limit, controlling the stress start of non-linear viscoelasticity; σ_{vM} is the von Mises equivalent stress:

$$\sigma_{vM}(\tau) = \sqrt{\frac{3}{2}\boldsymbol{s}(\tau) : \boldsymbol{s}(\tau)} \tag{10}$$

where $\boldsymbol{s}(\tau)$ denotes the deviatoric part of stress. At time t, $\sigma_{vM}^{\max}$ denotes the maximum value of von Mises stress during its history up to time t, that is:

$$\sigma_{vM}^{\max} = \sup_{\tau \leqslant t} \sigma_{vM}(\tau) \tag{11}$$

By using ramp function, the model is capable of describing the material's linear response when the stress is sufficiently small, in other words, less than the linear viscoelastic stress limit.

There are some major differences between Schapery's nonlinear viscoelastic model recalled in subsection 2.1 and our proposal, and these differences make the latter more suitable for cyclic loading. Firstly, in the 3D version of Schapery's model -e.g., Kim and Muliana (2009)-the nonlinear stress functions depend on the current value of the von Mises stress at time t, i.e. $\sigma_{vM}(t)$ while in the proposed model, they depend on the maximum value reached by the von Mises stress up to time t, i.e. $\sup_{\tau \leqslant t} \sigma_{vM}(\tau)$. Secondly, except for stress function g_1 which plays a similar role to that of $\widehat{g}_2$ in Schapery's model, the two models are written very differently. Indeed, in Schapery's model the hereditary integral is multiplied with stress function $\widehat{g}_1$ and the viscoelastic moduli are computed at reduced times $\psi(t)$, see Eqs. (1) and (2). In our proposal, the relaxation times are multiplied by nonlinear stress function g_2, see Eqs. (7) and (8).

3. Numerical implementation

In order to validate the proposed model against experimental tests, the model was implemented into the commercial finite element package ABAQUS® through user-defined material subroutine UMAT. The UMAT allows to define the stress-strain response of materials and it requires the updates of stress, Jacobian matrix and solution-dependent state variables.

After manipulating Equations (6) and (7), the stress components could be expressed as:

$$\begin{cases} \boldsymbol{s}(t) = \boldsymbol{s}\quad(t) + \sum_{i=1}^{I} \boldsymbol{s}_i(t) \\ \sigma_H(t) = \sigma_{H_\infty}(t) + \sum_{j=1}^{J} \sigma_{H_j}(t) \end{cases} \tag{12}$$

where

$$\begin{cases} \boldsymbol{s}\quad(t) = 2G\quad g_1(t)\boldsymbol{\xi}(t) \\ \boldsymbol{s}_i(t) = 2G_i g_1(t) \int_{-}^{t}\quad \exp\left(-\frac{t-\tau}{\tau_i^G g_2(t)}\right) \frac{\partial \boldsymbol{\xi}(\tau)}{\partial \tau} \mathrm{d}\tau \\ \sigma_{H_\infty}(t) = 3K\quad g_1(t)\varepsilon_H(t) \\ \sigma_{H_j}(t) = 3K_j g_1(t) \int_{-}^{t}\quad \exp\left(-\frac{t-\tau}{\tau_j^K g_2(t)}\right) \frac{\partial \varepsilon_H(\tau)}{\partial \tau} \mathrm{d}\tau \end{cases} \tag{13}$$

Since stress functions $g_1(\sigma(t))$ and $g_2(\sigma(t))$ in Equation (8) are dependent on the maximum value of von Mises stress during the history, they may dependent on the current stress value at time t, which is unknown yet. Let us designate their values at t as $g_1(t)$ and $g_2(t)$. Given a time interval $[t^n, t^{n+1}]$

and strain increment $\triangle\boldsymbol{\xi}$, $\boldsymbol{s}\ \ (t)$ at t^{n+1} becomes

$$\boldsymbol{s}\ \ \left(t^{n+1}\right) = \frac{g_1\left(t^{n+1}\right)}{g_1\left(t^{n}\right)}\left(\boldsymbol{s}\ \ \left(t^{n}\right) + 2G\ \ g_1\left(t^{n}\right)\triangle\boldsymbol{\xi}\right) \tag{14}$$

while

$$\begin{aligned}\boldsymbol{s}_i\left(t^{n+1}\right) =& 2G_i g_1\left(t^{n+1}\right)\int_{-}^{t^n}\exp\left(-\frac{t^{n+1}-\tau}{\tau_i^G g_2\left(t^{n+1}\right)}\right)\frac{\partial\boldsymbol{\xi}(\tau)}{\partial\tau}\mathrm{d}\tau\\ &+ 2G_i g_1\left(t^{n+1}\right)\int_{t^n}^{t^{n+1}}\exp\left(-\frac{t^{n+1}-\tau}{\tau_i^G g_2\left(t^{n+1}\right)}\right)\frac{\partial\boldsymbol{\xi}(\tau)}{\partial\tau}\mathrm{d}\tau\end{aligned} \tag{15}$$

As mentioned above, $g_1(t^{n+1})$ may depend on the yet unknown stress at t^{n+1}, which adds considerable complexity to the algorithm. Therefore, we make the simplified assumption: $g_1(t^{n+1}) \approx g_1(t^n)$ and $g_2(t^{n+1}) \approx g_2(t^n)$. Equations (14) and (15) become:

$$\begin{cases}\boldsymbol{s}\ \ \left(t^{n+1}\right) \approx \boldsymbol{s}\ \ \left(t^{n}\right) + 2G\ \ g_1\left(t^{n}\right)\triangle\boldsymbol{\xi}\\ \boldsymbol{s}_i\left(t^{n+1}\right) \approx \exp\left(-\frac{t}{\tau_i^G g_2(t^n)}\right)\boldsymbol{s}_i\left(t^{n}\right) + 2G_i g_1\left(t^{n}\right)\int_{t^n}^{t^{n+1}}\exp\left(-\frac{t^{n+1}-\tau}{\tau_i^G g_2(t^n)}\right)\frac{\partial\boldsymbol{\xi}(\tau)}{\partial\tau}\mathrm{d}\tau\end{cases} \tag{16}$$

We suppose that the viscoelastic strain rate is constant over the time interval (Chung and Ryou, 2009; Saleeb et al., 2001):

$$\frac{\partial\boldsymbol{\epsilon}(\tau)}{\partial\tau} = \text{ constant}, \quad \forall\tau|t^n < \tau \leqslant t^{n+1} \tag{17}$$

Consequently, if we set:

$$\triangle t = \frac{\triangle t}{g_2\left(t^n\right)} \tag{18}$$

$\boldsymbol{s}_i(t^{n+1})$ writes

$$\begin{aligned}\boldsymbol{s}_i\left(t^{n+1}\right) \approx& \exp\left(-\frac{\triangle t}{\tau_i^G}\right)\boldsymbol{s}_i\left(t^{n}\right)\\ &+ 2G_i\tau_i^G g_1\left(t^{n}\right)\left(1-\exp\left(\frac{-\triangle t}{\tau_i^G}\right)\right)\frac{\triangle\boldsymbol{\xi}}{\triangle t}\end{aligned} \tag{19}$$

Similarly, for hydrostatic part, its expressions are as follows:

$$\left\{\begin{array}{l} \sigma_{H_\infty}\left(t^{n+1}\right) \approx \sigma_{H_\infty}\left(t^n\right)+3K \quad g_1\left(t^n\right) \triangle\varepsilon_H \\ \sigma_{H_j}\left(t^{n+1}\right) \approx \exp\left(-\frac{\Delta \tilde{t}}{\tau_j^K}\right) \sigma_{H_j}\left(t^n\right)+3K_j\tau_j^K g_1\left(t^n\right)\left(1-\exp\left(\frac{- \quad \tilde{t}}{\tau_j^K}\right)\right) \frac{\varepsilon_H}{\Delta \tilde{t}} \end{array}\right. \tag{20}$$

we introduce the notation

$$\left\{\begin{array}{l} G(\triangle t) \equiv G \quad + \sum_{i=1}^{I} G_i G_i(\triangle t) \\ K(\triangle t) \equiv K \quad + \sum_{j=1}^{J} K_j K_j(\triangle t) \end{array}\right. \tag{21}$$

with

$$\left\{\begin{array}{l} G_i(\triangle t) \equiv \left(1-\exp\left(-\frac{\tilde{t}}{\tau_i^G}\right)\right) \frac{\tau_i^G}{\tilde{t}} \\ K_j(\triangle t) \equiv \left(1-\exp\left(-\frac{\tilde{t}}{\tau_j^K}\right)\right) \frac{\tau_j^K}{\tilde{t}} \end{array}\right. \tag{22}$$

Then finally, the update of stress is obtained as

$$\begin{aligned} \boldsymbol{\sigma}\left(t^{n+1}\right) \approx \boldsymbol{\sigma} \quad & \left(t^n\right)+g_1\left(t^n\right) \mathbb{C}^{ve}(\triangle t) : \triangle \boldsymbol{\epsilon}+\sum_{i=1}^{I} \exp\left(-\frac{\triangle t}{\tau_i^G}\right) \boldsymbol{s}_i\left(t^n\right) \\ & +\sum_{j=1}^{J} \exp\left(-\frac{\triangle t}{\tau_j^K}\right) \sigma_{H_j}\left(t^n\right) \boldsymbol{I} \end{aligned} \tag{23}$$

where $\mathbb{C}^{ve}(\triangle t)$ is defined as:

$$\mathbb{C}^{ve}(\triangle t)=2G(\triangle t)\mathbb{I}^{dev}+3K(\triangle t)\mathbb{I}^{vol} \tag{24}$$

Jacobian matrix is expressed in following form:

$$\boldsymbol{C}=\frac{\partial \boldsymbol{\sigma}\left(t^{n+1}\right)}{\partial \boldsymbol{\epsilon}\left(t^{n+1}\right)} \tag{25}$$

and is obtained as:

$$\boldsymbol{C}=g_1\left(t^n\right) \mathbb{C}^{ve}(\triangle t) \tag{26}$$

The nonlinear history-dependent stress functions $g_1(t)$ and $g_2(t)$ need to be updated over every time interval. In UMAT, we defined a solution-dependent variable to test whether the current von Mises stress $\sigma_{vM}(t^n)$ exceeds the σ_{vM}^{max}. If so, this variable is updated; if not, it keeps the same value until next step. After σ_{vM}^{max} is updated, $g_1(t^n)$ and $g_2(t^n)$ are updated as well.

4. Application of the model to HTPB propellant

In this section, the proposed constitutive model is applied to predict the behavior of a solid composite propellant under various cyclic loading conditions and compared with the experimental data.

4.1. Materials and tests

The investigated HTPB (hydroxyl-terminated polybutadiene) propellant is a particle-filled composite polymer composed of 17-wt.% Al (aluminum), 70-wt.% AP (ammonium perchlorate), and 13-wt.% of a HTPB matrix and other additives. The microstructure of HTPB propellant was observed by a scanning electron microscope and is shown in Fig. 1. The figure reveals that large AP particles and small Al particles are distributed randomly in the HTPB matrix. Displacement-controlled sinusoidal fatigue tests of HTPB propellant with a nominal strain ratio R (ratio between the minimum and the maximum applied strains) equal to -1 were conducted under room temperature of 23°C with various frequencies and strain amplitudes by a dynamic mechanical analyzer, DMA-ELF3200 (manufactured by BOSE®, USA, see Fig. 2). Experimental methodology, procedures and results may be found in Tong et al. (2017, 2018).

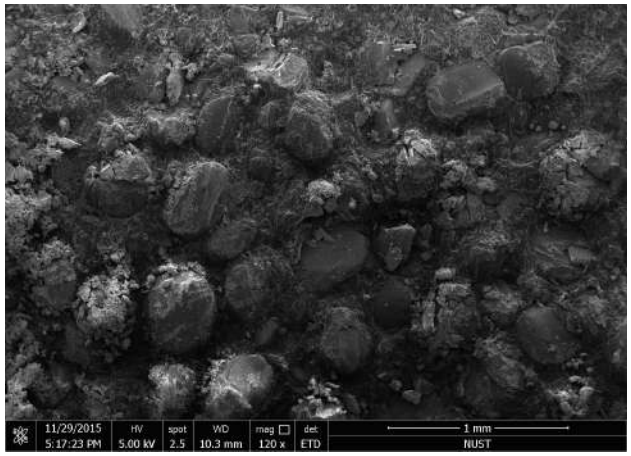

Figure 1: Microstructure of HTPB propellant (120x magnification).

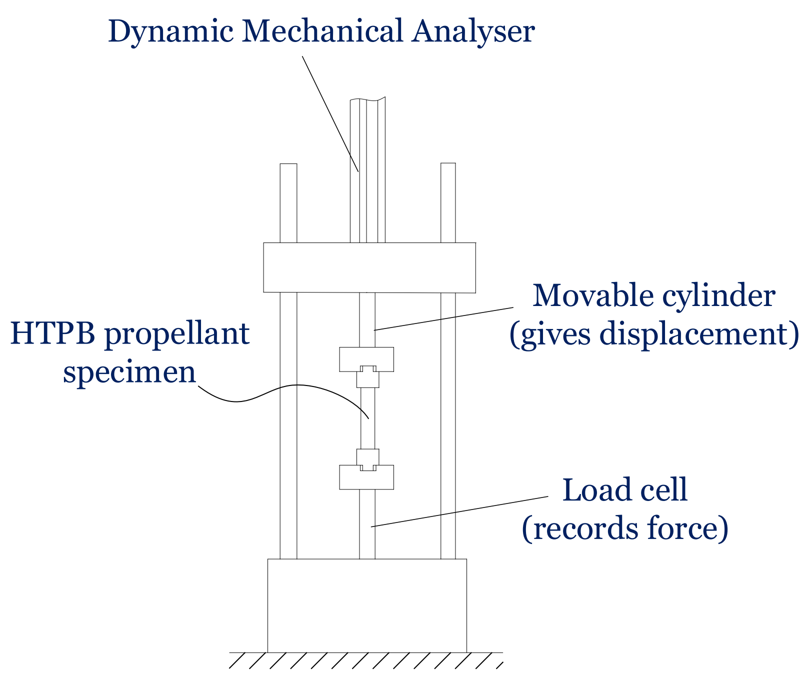

Figure 2: Illustration of dynamic mechanical analyzer.

4.2. Model calibration

4.2.1. Identification of viscoelastic parameters

The linear viscoelastic parameters need to be determined by obtaining the relaxation moduli of the material. Some investigators have applied DMA test to capture the dynamic viscoelastic response of polymeric materials (Park and Schapery, 1999). For a deformation-controlled uniaxial stress experiment, the strain and stress could be expressed as follows:

$$\varepsilon(t) = \varepsilon_0 \mathrm{e}^{\mathrm{i}\omega t},\ \ \sigma(t) = f(\varepsilon(t)) \tag{27}$$

where ε_0 is the amplitude of deformation of the harmonic oscillation and ω is the angular frequency. The dynamic modulus is the ratio of stress to strain: $E^*(\omega) = \sigma(t)/\varepsilon(t)$. Using the response to a steady state sinusoidal loading, $E^*(\omega)$ can be rewritten as a sum:

$$E^*(\omega) = E\ (\omega) + \mathrm{i}E\ \ (\omega) \tag{28}$$

where the real part $E\ (\omega)$ is defined as the storage modulus and the imaginary part $E\ \ (\omega)$ as the loss modulus. The relaxation modulus is generally expressed as a Prony series in time domain:

$$E(t) = E\quad + \sum_{i=1}^{I} E_i \exp\left(-\frac{t}{\tau_i}\right) \tag{29}$$

By using the Laplace-Carson transform, we can write:

$$E(s) \equiv s \int_0 \quad E(t)\mathrm{e}^{-st}\mathrm{d}t = E\quad + \sum_{i=1}^{I} \frac{E_i s}{s + \frac{1}{\tau_i}} \tag{30}$$

If we take $s = \mathrm{i}\omega$, the previous equation becomes:

$$E^*(\omega) = E(\mathrm{i}\omega) = E\quad + \sum_{i=1}^{I} \frac{E_i \omega^2}{\omega^2 + \left(\frac{1}{\tau_i}\right)^2} + \mathrm{i}\left(\sum_{i=1}^{I} \frac{E_i \frac{\omega}{\tau_i}}{\omega^2 + \left(\frac{1}{\tau_i}\right)^2}\right) \tag{31}$$

To identify the viscoelastic parameters (E_i, τ_i and $E\ \ $), we used the least squares method by minimizing the sum of squared residuals according to Equation (31). In this application, the residual is the difference between experimental results obtained by DMA at room temperature 23°C and analytical predictions of the loss and storage moduli, see Fig. 3. In the literature, up to $I = 20$ relaxation times are used (Ciambella et al., 2010); however a large value of I could lead to ill-conditioned identification problems. In the present study, $I = 7$ is shown to have best fitting result. The identified material parameters are listed in Table 1, with $E_0 = E \quad + \sum_{i=1}^{I} E_i$.

Due to the limits of experimental apparatus, it was not possible to directly identify the time-dependent shear and bulk moduli $G(t)$ and $K(t)$ for HTPB propellant. It is more appropriate to use Prony series for $G(t)$ and $K(t)$ directly determined from multiaxial experimental data. However, if the only available data is uniaxial test, $G(t)$ and $K(t)$ could be derived from $E(t)$ and estimated from the following relations (a similar approach has been applied in Miled et al. (2011)):

$$\left\{ \begin{array}{lll} G = \frac{E_\infty}{2(1+v)}, & G_i = \frac{E_i}{2(1+v)}, & \tau_i^G = \frac{\tau_i E_i}{G_i} \\ K = \frac{E_\infty}{3(1-2v)}, & K_i = \frac{E_i}{3(1-2v)}, & \tau_i^K = \frac{\tau_i E_i}{K_i} \end{array} \right. \text{(no sum)} \tag{32}$$

where v is Poisson's ratio. It is known that for polymers, Poisson's ratio cannot generally be considered as a material parameter (Tschoegl et al., 2002). However, as there is no sufficient experimental data, here it is assumed that v is constant and equal to 0.495 for HTPB propellant (according to the work of Jung and Youn (1999), the solid composite propellant is supposed to experience a nearly incompressible state subjected to small strain tension, which supports the choice of a nearly incompressible value (0.495) for Poisson's ratio of HTPB propellant).

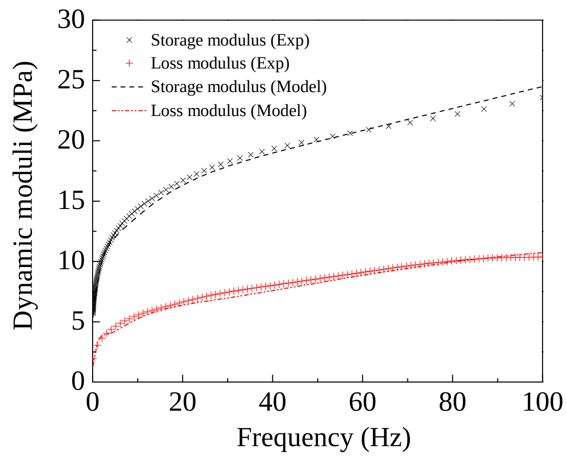

Figure 3: Experimental and analytical results of storage and loss moduli for HTPB propellant at 23°C.

Table 1: Prony series of HTPB propellant's relaxation modulus.

i	E_i (MPa)	τ_i (s)
1	21.2635	1×10^{-3}
2	6.7852	1×10^{-2}
3	5.3457	1×10^{-1}
4	1.5882	1×10^{0}
5	1.3455	1×10^{1}
6	1.0000	1×10^{2}
7	1.0000	1×10^{3}
$E_0 = 39.9132$ (MPa)		

4.2.2. Identification of linear viscoelastic stress limit

When subjected to considerably small loading, weak debonding at matrix/particle interface or small micro-cracks of matrix inside the composite propellant occur. The mechanical behavior of the composite propellant can be considered to comply with linear viscoelastic theory under such circumstances. The linear viscoelastic stress limit (σ_0, defined in subsection 2.2) is a critical value that distinguishes between linear and nonlinear viscoelasticity. In terms of uniaxial tensile loading, the characteristic linear stress-strain curve can be considered to be obtained within the linear viscoelastic range of the material, reflecting the mechanical properties with little damage. In order to better obtain the stress limit in fatigue test, we compared the linear viscoelastic predicted result (with viscoelastic parameters in Table 1) against experimental data. A representative comparison is presented in Fig. 9. As long as the experimental stress-strain curve and the linear one coincide with each other, it can be deduced that the material deforms in a linear viscoelastic mode. When there is a deviation, the material starts to suffer from damage, leading to the nonlinearity of the mechanical response. The stress value, corresponding to the data where the linear characteristic curve and the actual one begin to deviate, can be considered as the linear viscoelastic stress limit. This will be illustrated in the next subsection.

4.2.3. Identification of nonlinear history-dependent stress functions

Functions $g_1(\sigma)$ and $g_2(\sigma)$ in Equation (8) depend on the history of von Mises equivalent stress, however, before the calibration procedure, we set some fixed values of g_1 and g_2 and then applied them in nonlinear constitutive model to simulate the hysteresis loops. The simulations were thus evaluated by comparing with experimental data, to assess the impact of g_1 and g_2 upon the changes of slopes and areas of hysteresis loops. The results indicated that g_1 and g_2 should be both less than 1.0 to approach the real experimental data. In order to precisely identify the parameters of the two functions, we narrow the ranges of values of parameters by a preliminary analysis on the nonlinear functions g_1 and g_2. The results of identification procedure reveal that:

$$k_1 < 0,\ 0 < m_1 < 1,\ 0 < k_2 < 1,\ 0 < m_2 < 1,\ 0 < C_2 < 1 \tag{33}$$

Due to the fact that the model is temperature independent, calibration of nonlinear functions should be accomplished under isothermal condition. Nevertheless, the self-heating effect was inevitable in the course of cyclic loading. In order to reduce the impact of self-heating on the stress-strain relation (hysteresis loop), we chose the smallest frequency and strain amplitude among our experimental results, under which the self-heating effect could be ignored. Hence the experimental data set with applied strain amplitude 0.01 and frequency 1 Hz was chosen. Figure 4 shows the temperature increment of HTPB propellant during fatigue and it proves that the data set we selected is reasonable because of a minimum temperature increment of 0.2°C.

Any three-dimensional constitutive equations should be able to correctly describe the material response under one-dimensional conditions, so numerical simulations for uniaxial loading can be used to assess the validity of the model and numerical algorithm. The operation of obtaining parameters is accomplished with one brick element model in ABAQUS (element type is C3D8).

We adjusted the parameters k_1, m_1, k_2, m_2 and C_2 one by one to approximately find their optimal value. By repeatedly running the UMAT with above parameters after the tolerance error of simulated hysteresis loop was met (error was defined as the difference of stresses between predicted and experimental results), accurate parameters in Table 2 were obtained.

The stress variation with the number of cycles for HTPB propellant under $f = 1$ Hz and $\varepsilon_a = 0.01$ is presented in Fig. 5. The model was calibrated against all 20 experimental cycles in Fig. 5, which shows that good agreement between model calibration and experimental data is met. A representative tenth hysteresis loop shown in Fig. 6 further proves that excellent calibration result is achieved. The impact of each parameter upon the stress-strain response was also clarified: k_1, m_1, k_2 and m_2 mainly control the slope of the loop while C_2 controls the area and slope of hysteresis loop, and is very sensitive to minor changes, see Fig. 7.

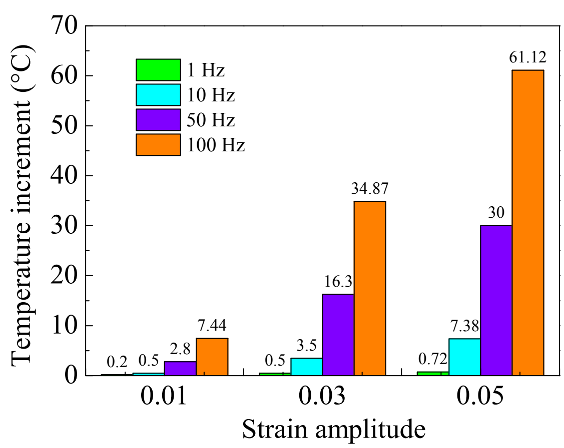

Figure 4: Temperature increment of HTPB propellant during fatigue above the room temperature of 23°C (quoted from Tong et al. (2018))

.

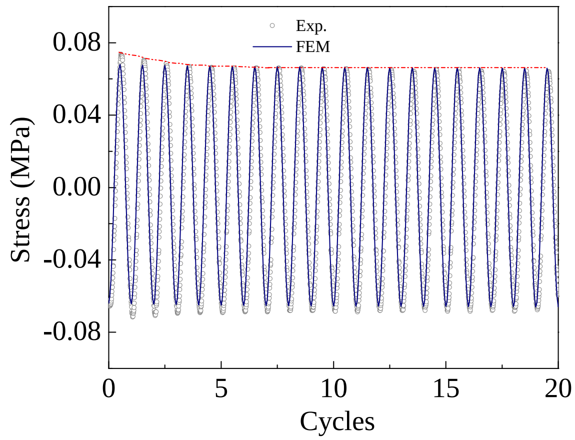

Figure 5: Stress variation with number of cycles for HTPB propellant (with $f = 1$ Hz and $\varepsilon_a = 0.01$).

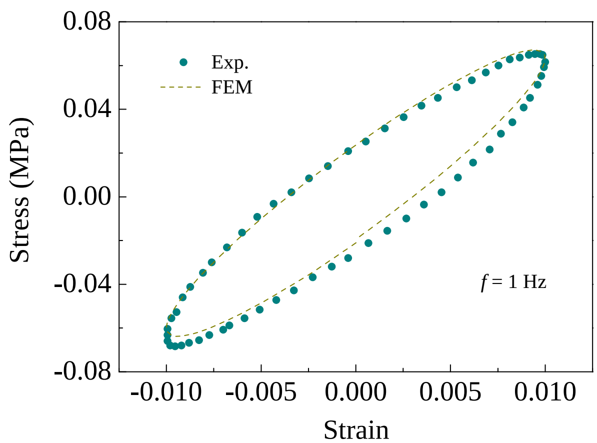

Figure 6: Calibration of parameters of nonlinear history-dependent stress functions (tenth cycle).

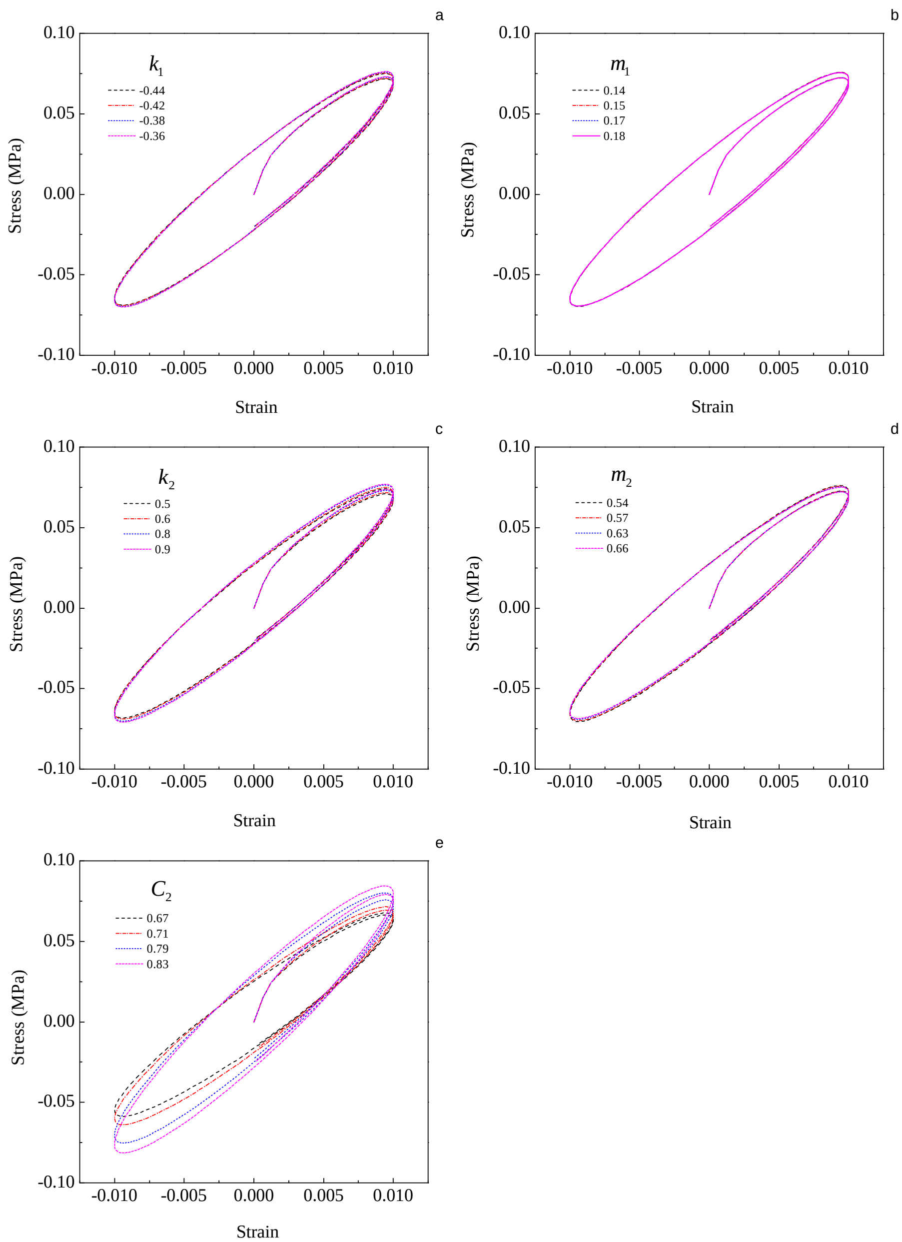

Figure 7: Sensitivity analysis of calibrated parameters of history-dependent nonlimear stress functions.

Table 2: Parameters of nonlinear viscoelastic functions.

k_1	m_1	k_2	m_2	C_2
-0.40	0.16	0.70	0.60	0.725

The evolution of history-dependent nonlinear stress functions g_i after calibration is presented in Fig. 8, which shows that g_1 and g_2 are both less than 1.0 in nonlinear viscoelastic domain and decrease with increasing maximum von Mises stress. The comparison of the linear (LVE) and nonlinear (NLVE) viscoelastic model is shown in Fig. 9. It is clear from the figure that the deviation from linearity starts at a stress of 0.012 MPa, which is defined as the linear viscoelastic stress limit. Figure 9 also shows that linear viscoelasticity is unable to reproduce the hysteresis loop, and even the mean slope of the loop is completely missed by the linear model.

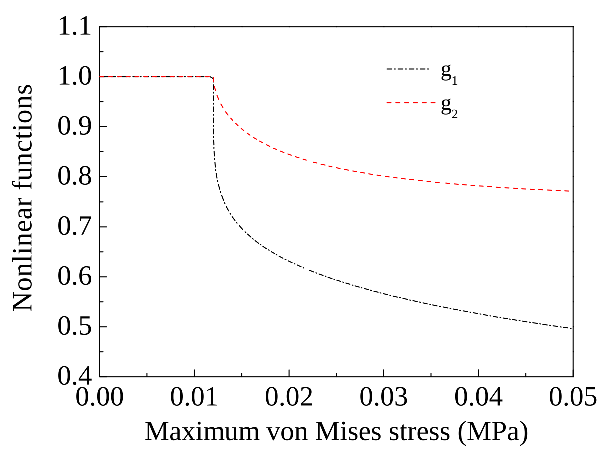

Figure 8: History-dependent nonlinear stress functions after calibration for HTPB propellant (with $f = 1$ Hz and $\varepsilon_a = 0.01$).

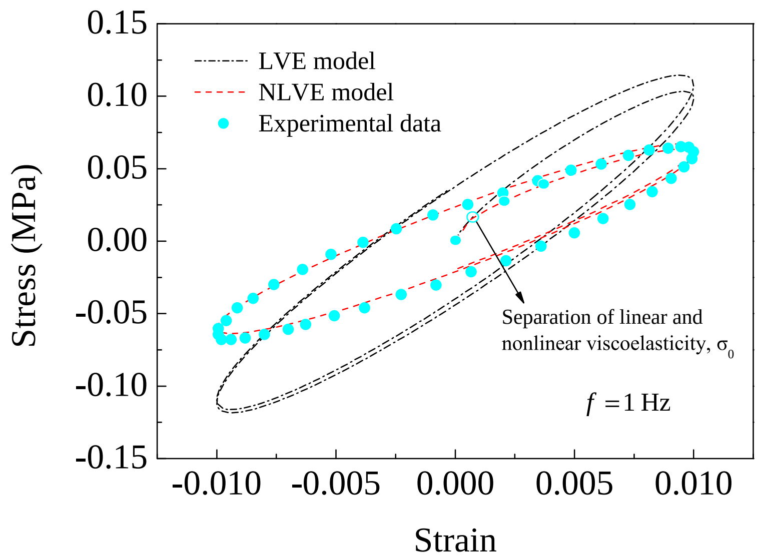

Figure 9: Comparison of predictions of the linear (LVE) and nonlinear (NLVE) viscoelastic models against experimental data (with $f = 1$ Hz and $\varepsilon_a = 0.01$).

4.3. Model validation

Numerical results presented in Figs. 5 to 9 all pertain to $f = 1$ Hz and $\varepsilon_a = 0.01$ and were obtained from the model parameter values of Table 2 which were calibrated from Fig. 5. In this section, the same set of calibrated parameters will be used to predict results for other frequencies and strain amplitudes. The capability of the proposed constitutive model and numerical algorithm is evaluated by comparing FEM simulation with experimental results that were not used in the model parameter identification. The simulated physical model was designed according to the geometry of the tested HTPB propellant specimen, illustrated in Fig. 10. The element type used in simulation is C3D8 and the analysis step is quasi-static. Figure

11 shows the predicted results versus experimental data of hysteresis loops at the tenth cycle, after which hysteresis loop remains stable and does not change anymore.

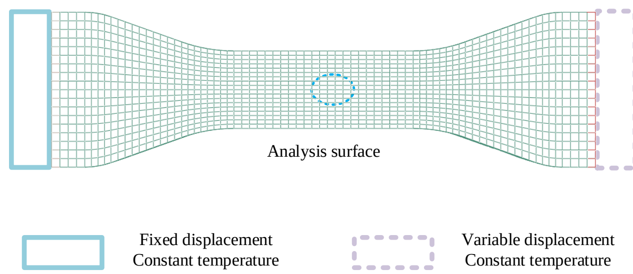

Figure 10: Illustration of the physical model in Abaqus. Note that gauge length of the specimen is 15 mm and thickness of the specimen is 5 mm.

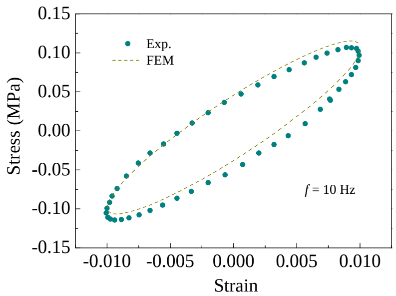

(a) $f = 10$ Hz, $\varepsilon_a = 0.01$

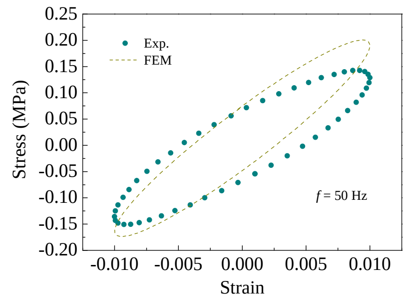

(b) $f = 50$ Hz, $\varepsilon_a = 0.01$

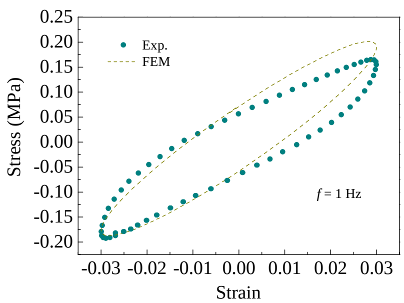

(c) $f = 1$ Hz, $\varepsilon_a = 0.03$

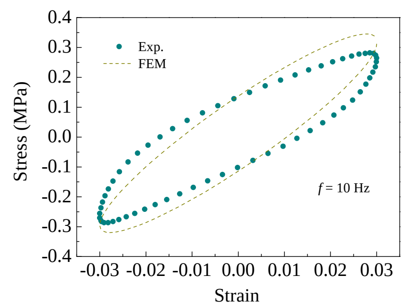

(d) $f = 10$ Hz, $\varepsilon_a = 0.03$

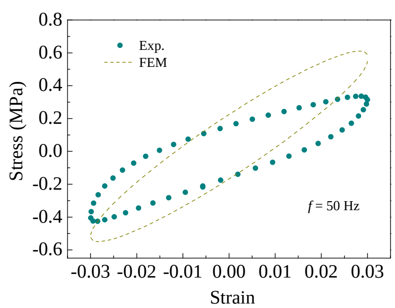

(e) $f = 50$ Hz, $\varepsilon_a = 0.03$

Figure 11: Comparison of experimental and simulation results using the material parameters in Table 2 (10^{th} cycle).

From the figure, it is found that the experimental hysteresis loops are qualitatively reproduced. In order to analyze the predictive capacity of proposed model, the mean slope of the hysteresis loop (the slope of stress versus strain, $\Delta\sigma/\Delta\epsilon$) was selected as a first indicator. Figure 12 provides the error on the slopes of predicted hysteresis loops with respect to experimental data. The error is defined as:

$$Error = \left| \frac{FEM(slope) - Exp(slope)}{Exp(slope)} \right| \times 100\% \tag{34}$$

Figure 12 proves that, for smaller strain amplitude and frequency (see Figs. 11(a) and 11(c)), clearly, the model predictions are in close agreement with the test data and the slopes are more consistent with each other (see Fig. 12).

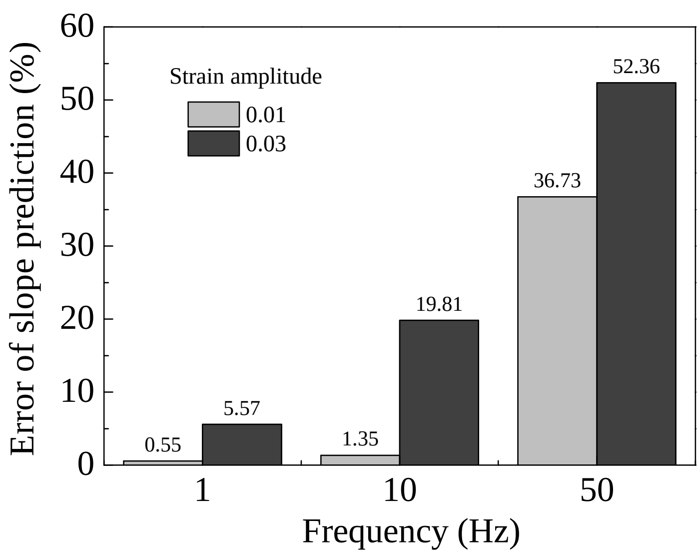

Figure 12: Error of slopes of experimental and simulation results.

The area of hysteresis loop expresses the dissipated energy alongside fatigue process. Likewise, we compared the error of areas of experimental and simulated ones, as illustrated in Fig. 13. In the figure, errors on the areas under various strain amplitudes and frequencies reveal that even if the predicted slope matches closely with the experimental one, the prediction of dissipated energy would not be as well as that of slope.

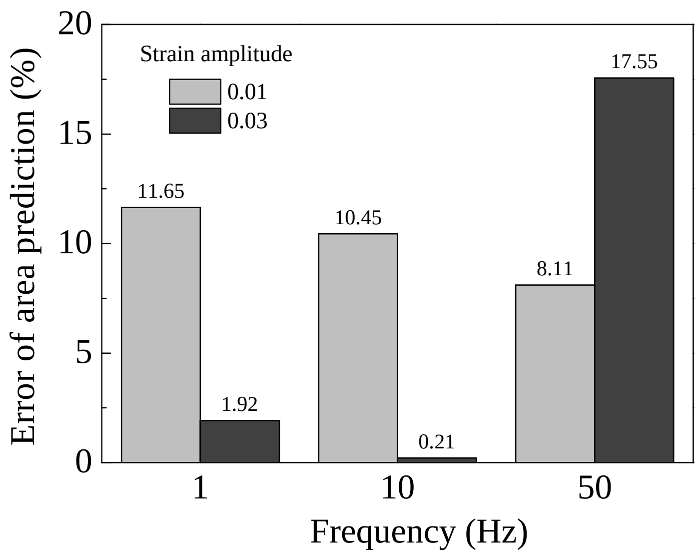

Figure 13: Error of areas of experimental and simulation results.

5. Discussion

By proposing a nonlinear viscoelastic constitutive model using two history-dependent stress functions, we successfully modified the conventional Schapery-type model and then applied it to reproduce the cyclic behavior of a solid composite propellant at room temperature. As compared to the experimental data, the proposed model was able to capture the main characteristics of cyclic responses of HTPB propellant under small strain amplitudes and frequencies (e.g., $\varepsilon_a = 0.01$ and $f = 10$ Hz; $\varepsilon_a = 0.03$ and $f = 1$ Hz). In these cases, the impact of self-heating upon the mechanical properties could be ignored. In this study, the predictive capability of the nonlinear model is mainly validated against the experimentally measured slopes of the stress-strain hysteresis loops, whereas the measured loop areas are not well predicted. There are cases also where the shape of the loops is not correctly simulated.

The poor predictions regarding the loop slopes or areas may originate from temperature variation during fatigue. When the heat dissipation during fatigue, or self-heating effect, is excited by mechanical loading, the temperature of HTPB propellant experiences rapid increase at the initial stage and subsequent long-term stability due to heat equilibrium between the specimen and the environment. As far as we know, self-heating is crucial for dynamically loaded polymers (Rittel, 2000; Montesano et al., 2013; Le Cam, 2017). Subjected to cyclic loading, the HTPB propellant is softened by increasing temperature, causing the slope of the hysteresis loop to decrease as a result of temperature sensitivity. Since the present constitutive model is derived from an isothermal framework and does not account for self-heating, the mean slopes during loading-unloading phase are overestimated, causing differences between experimental data and model predictions. Due to the fact that we did not consider self-heating in the present model, the predicted slopes of hysteresis loops are generally larger than real ones. It is expected that if we further extend the model to a coupled thermo-mechanical one, predictions of experimental results for larger frequencies and strain amplitudes (e.g. test data sets $f = 50$ Hz and $\varepsilon_a = 0.01$; $f = 10$ Hz and $\varepsilon_a = 0.03$) will be significantly improved.

Regarding the shape of the hysteresis loops, Figs. 11 (a)-(e) show that the model predicts elliptical shapes. Experimentally, this seems to be the case for small strain amplitudes (Figs. 11(a)-(b)) while at larger strain amplitudes, the experimental loops become distorted and the distortion increases with the frequency (Figs. 11(c)-(d)). We believe that this is due to the nonlinear stress functions in subsection 2.2 depending on the history of the von Mises stress. The latter stress norm does not depend on the stress sign and its alternating change during cyclic tension-compression. However, the microstructure of the solid propellant leads to a response which is different in tension and compression, with tensile loads being able to lead to particle debonding and void growth in the polymer matrix, and this is exacerbated by repeated cyclic loading. There are two possible modeling solutions to this. The first is to develop a micro-mechanically based model which takes into account the microstructure and different damage mechanisms. An example of this approach is given in Brassart et al. (2009), but it needs to be enriched by replacing the hyperelastic model for the matrix with a nonlinear viscoelastic one. A second approach is to keep a phenomenological macroscopic model but to couple the viscoelastic response with a continuum damage model, as in Tunç and Özüpek (2017). Furthermore, the non-symmetric and distorted stress-strain loops in Figs. 11(c)-(e) suggest that damage accumulation leads to anisotropy, therefore a coupled nonlinear viscoelastic-damage model should be anisotropic and treat compressive and tensile principal (eigen) stresses differently. This could be achieved for instance by extending the anisotropic elastoplastic-damage model of Lemaitre et al. (2000).

Another limitation of the present model is its restriction to the small perturbation regime, while it is known that solid propellants may undergo large strains and/or rotations. Therefore, the model needs to be extended to the finite deformation regime, e.g. as in Tunç and Özüpek (2017).

6. Conclusions

A nonlinear viscoelastic constitutive model and corresponding numerical algorithm were proposed and then applied to simulate the cyclic responses of HTPB propellant. The key idea of the model was to introduce two functions which depend on the history of von Mises stress and affect the relaxation times and the strain history in the integral formulation of viscoelasticity.

The results proved the capability of predicting the nonlinear response under cyclic loading. Several conclusions are drawn here:

- The HTPB propellant experiences complex deformation pattern under cyclic loading, which leads to a stress-strain response far beyond the scope of linear viscoelasticity.
- By introducing history-dependent nonlinear stress functions, the cyclic stress-strain behavior of HTPB propellant is described. Good agreement with experimental data is met under quasi-isothermal conditions.
- The differences between the hysteresis loops predicted by the model and experimental results illustrate the impact of self-heating on the mechanical properties of HTPB propellant during fatigue process. Cur-

rent research of the authors focuses on the extension of the model to fully coupled thermo-mechanical conditions.

Acknowledgments

This work was funded by the National Natural Science Foundation of China (Grant No. 51606098). Xin Tong gratefully acknowledges the China Scholarship Council for financial support.

References

Al-Rub, R. K. A. and Darabi, M. K. (2012). A thermodynamic framework for constitutive modeling of time- and rate-dependent materials. part i: Theory. *International Journal of Plasticity*, 34:61 92.

Brassart, L., Inglis, H., Delannay, L., Doghri, I., and Geubelle, P. H. (2009). An extended mori tanaka homogenization scheme for finite strain modeling of debonding in particle-reinforced elastomers. *Computational Materials Science*, 45(3):611 616.

Chung, K. and Ryou, H. (2009). Development of viscoelastic/rate-sensitive-plastic constitutive law for fiber-reinforced composites and its applications. part i: Theory and material characterization. *Composites Science and Technology*, 69(2):284 291.

Ciambella, J., Paolone, A., and Vidoli, S. (2010). A comparison of nonlinear integral-based viscoelastic models through compression tests on filled rubber. *Mechanics of Materials*, 42(10):932 944.

Darabi, M. K., Al-Rub, R. K. A., Masad, E. A., Huang, C.-W., and Little, D. N. (2011). A thermo-viscoelastic-viscoplastic-viscodamage constitutive model for asphaltic materials. *International Journal of Solids and Structures*, 48(1):191 207.

Darabi, M. K., Al-Rub, R. K. A., Masad, E. A., and Little, D. N. (2012). A thermodynamic framework for constitutive modeling of time- and rate-dependent materials. part ii: Numerical aspects and application to asphalt concrete. *International Journal of Plasticity*, 35:67 99.

DeLuca, L., Galfetti, L., Maggi, F., Colombo, G., Merotto, L., Boiocchi, M., Paravan, C., Reina, A., Tadini, P., and Fanton, L. (2013). Characterization of htpb-based solid fuel formulations: Performance, mechanical properties, and pollution. *Acta Astronautica*, 92(2):150 162.

Drozdov, A. (2011). Cyclic strengthening of polypropylene under strain-controlled loading. *Materials Science and Engineering: A*, 528(29-30):8781 8789.

Guo, Q., Zaïri, F., and Guo, X. (2018). A thermo-viscoelastic-damage constitutive model for cyclically loaded rubbers. part i: Model formulation and numerical examples. *International Journal of Plasticity*, 101:106 124.

Haj-Ali, R. M. and Muliana, A. H. (2004). Numerical finite element formulation of the schapery non-linear viscoelastic material model. *International Journal for Numerical Methods in Engineering*, 59(1):25 45.

Hinterhoelzl, R. and Schapery, R. (2004). Fem implementation of a three-dimensional viscoelastic constitutive model for particulate composites with damage growth. *Mechanics of Time-Dependent Materials*, 8(1):65 94.

Huang, C.-W., Masad, E., Muliana, A. H., and Bahia, H. (2007). Nonlinearly viscoelastic analysis of asphalt mixes subjected to shear loading. *Mechanics of Time-Dependent Materials*, 11(2):91 110.

Jung, G.-D. and Youn, S.-K. (1999). A nonlinear viscoelastic constitutive model of solid propellant. *International Journal of Solids and Structures*, 36(25):3755 3777.

Kim, J. S. and Muliana, A. (2009). A time-integration method for the viscoelastic viscoplastic analyses of polymers and finite element implementation. *International Journal for Numerical Methods in Engineering*, 79(5):550 575.

Krairi, A. and Doghri, I. (2014). A thermodynamically-based constitutive model for thermoplastic polymers coupling viscoelasticity, viscoplasticity and ductile damage. *International Journal of Plasticity*, 60:163 181.

Lai, J. and Bakker, A. (1995). An integral constitutive equation for nonlinear plasto-viscoelastic behavior of high-density polyethylene. *Polymer Engineering and Science*, 35(17):1339 1347.

Lai, J. and Bakker, A. (1996). 3-d schapery representation for non-linear viscoelasticity and finite element implementation. *Computational Mechanics*, 18(3):182 191.

Le Cam, J.-B. (2017). Energy storage due to strain-induced crystallization in natural rubber: the physical origin of the mechanical hysteresis. *Polymer*, 127:166 173.

Lemaitre, J., Desmorat, R., and Sauzay, M. (2000). Anisotropic damage law of evolution. *European Journal of Mechanics A-solids*, 19(2):187 208.

Miled, B., Doghri, I., and Delannay, L. (2011). Coupled viscoelastic viscoplastic modeling of homogeneous and isotropic polymers: Numerical algorithm and analytical solutions. *Computer Methods in Applied Mechanics and Engineering*, 200(47-48):3381 3394.

Montesano, J., Fawaz, Z., and Bougherara, H. (2013). Use of infrared thermography to investigate the fatigue behavior of a carbon fiber reinforced polymer composite. *Composite Structures*, 97:76 83.

Muliana, A. H. and Haj-Ali, R. (2008). A multi-scale framework for layered composites with thermo-rheologically complex behaviors. *International Journal of Solids and Structures*, 45(10):2937 2963.

Muliana, A. H. and Haj-Ali, R. M. (2006). Analysis for creep behavior and collapse of thick-section composite structures. *Composite Structures*, 73(3):331 341.

Müller, S., Kästner, M., Brummund, J., and Ulbricht, V. (2011). A non-linear fractional viscoelastic material model for polymers. *Computational Materials Science*, 50(10):2938 2949.

Park, S. and Schapery, R. (1999). Methods of interconversion between linear viscoelastic material functions. part i a numerical method based on prony series. *International Journal of Solids and Structures*, 36(11):1653 1675.

Rittel, D. (2000). An investigation of the heat generated during cyclic loading of two glassy polymers. part i: Experimental. *Mechanics of Materials*, 32(3):131 147.

Saleeb, A., Arnold, S., Castelli, M., Wilt, T., and Graf, W. (2001). A general hereditary multimechanism-based deformation model with application to the viscoelastoplastic response of titanium alloys. *International Journal of Plasticity*, 17(10):1305 1350.

Schapery, R. A. (1969). On the characterization of nonlinear viscoelastic materials. *Polymer Engineering & Science*, 9(4):295 310.

Tong, X., Chen, X., Xu, J., Sun, C., and Liang, W. (2017). Excitation of thermal dissipation of solid propellants during the fatigue process. *Materials & Design*, 128:47 55.

Tong, X., Chen, X., Xu, J.-s., Zheng, Y., and Zhi, S.-j. (2018). The heat build-up of a polymer matrix composite under cyclic loading: Experimental assessment and numerical simulation. *International Journal of Fatigue*, 116:323 333.

Tschoegl, N. W., Knauss, W. G., and Emri, I. (2002). Poisson's ratio in linear viscoelasticity a critical review. *Mechanics of Time-Dependent Materials*, 6(1):3 51.

Tunç, B. and Özüpek, Ş. (2016). Implementation and validation of a three dimensional damaging finite strain viscoelastic model. *International Journal of Solids and Structures*, 102:275 285.

Tunç, B. and Özüpek, Ş. (2017). Constitutive modeling of solid propellants for three dimensional nonlinear finite element analysis. *Aerospace Science and Technology*, 69:290 297.

Tunç, B., Özüpek, Ş., Podnos, E., and Arkun, U. (2019). Thermal cyclic stress analysis of a solid rocket motor. *Journal of Spacecraft and Rockets*, 56(1):179 189.

Xu, F., Aravas, N., and Sofronis, P. (2008). Constitutive modeling of solid propellant materials with evolving microstructural damage. *Journal of the Mechanics and Physics of Solids*, 56(5):2050 2073.